Geometry and network connectivity govern the mechanics of stress fibers

Elena Kassianidou[a,b], Christoph A. Brand[c,d], Ulrich S. Schwarz[c,d], and Sanjay Kumar[a,b,e,1]

[a]Department of Bioengineering, University of California, Berkeley, CA 94720; [b]UC Berkeley–UCSF Graduate Program in Bioengineering, University of California, Berkeley, CA 94720; [c]Institute for Theoretical Physics, Heidelberg University, 69120 Heidelberg, Germany; [d]BioQuant–Center for Quantitative Biology, Heidelberg University, 69120 Heidelberg, Germany; and [e]Department of Chemical and Biomolecular Engineering, University of California, Berkeley, CA 94720

Edited by Shu Chien, University of California, San Diego, La Jolla, CA, and approved January 12, 2017 (received for review April 27, 2016)

Actomyosin stress fibers (SFs) play key roles in driving polarized motility and generating traction forces, yet little is known about how tension borne by an individual SF is governed by SF geometry and its connectivity to other cytoskeletal elements. We now address this question by combining single-cell micropatterning with subcellular laser ablation to probe the mechanics of single, geometrically defined SFs. The retraction length of geometrically isolated SFs after cutting depends strongly on SF length, demonstrating that longer SFs dissipate more energy upon incision. Furthermore, when cell geometry and adhesive spacing are fixed, cell-to-cell heterogeneities in SF dissipated elastic energy can be predicted from varying degrees of physical integration with the surrounding network. We apply genetic, pharmacological, and computational approaches to demonstrate a causal and quantitative relationship between SF connectivity and mechanics for patterned cells and show that similar relationships hold for nonpatterned cells allowed to form cell–cell contacts in monolayer culture. Remarkably, dissipation of a single SF within a monolayer induces cytoskeletal rearrangements in cells long distances away. Finally, stimulation of cell migration leads to characteristic changes in network connectivity that promote SF bundling at the cell rear. Our findings demonstrate that SFs influence and are influenced by the networks in which they reside. Such higher order network interactions contribute in unexpected ways to cell mechanics and motility.

cytoskeleton | active cable model | actin | myosin | cell migration

Actomyosin stress fibers (SFs) enable mammalian cells to generate traction forces against the extracellular matrix (ECM) (1–3). These forces are increasingly recognized to play central roles in the regulation of cell shape, migration, and stem cell fate decisions (1, 4). At the multicellular level, these forces also contribute significantly to tissue morphogenesis, wound healing, and neoplasia (5, 6). SFs are composed of F-actin; structural proteins such as α-actinin; and frequently, nonmuscle myosin II (NMMII) (2, 7). When NMMII filaments are present, these structures generate tension that is transmitted along the length of the SF to ECM adhesions, surrounding SFs, and other connected structural elements such as the actin cortex, microtubules, intermediate filaments, and the nucleus (8). As such, SFs are capable of acting both locally and globally through their networked interactions with other cellular structures to impose tensile loads within the cell (9). This notion is a critical yet largely unexplored linchpin in current models of cell motility, where specific SF subsets are thought to coordinate tensile activities to direct remodeling of ECM adhesions and sculpt migratory processes (1, 10, 11).

The increasing appreciation of SFs as important players in cell mechanics and motility has stimulated great interest in measuring the contractile properties of individual SFs. Several techniques have been used over the past 2 decades, spanning two broad categories. The first and more reductionist category includes characterization of SFs extracted from cells (12) or reconstituted from molecular components (13). The second category includes characterization of SFs in living cells using tools such as subcellular laser ablation (SLA), which allows for the mechanical interrogation of single SFs (3). We and others have applied SLA to determine the viscoelastic contraction of sarcomeric structures within SFs (14–16) and tension distribution after SF ablation to focal adhesions (FAs) throughout the cell (9). Moreover, SLA has been used to spatially map SF viscoelastic properties within the cell and associate activities of specific NMMII activators and isoforms to these subpopulations (17, 18).

An important, emergent theme from these studies is that the effective mechanical contributions of an SF depend strongly on its geometry and structural context, although these relationships remain largely uninvestigated and controversial. Cellular heterogeneity represents a critical barrier to clarifying this, because cultured cells adopt a variety of morphologies giving rise to a poorly controlled diversity of SF geometries. Thus, it is challenging to understand fundamental material properties of SFs, including how length and ECM adhesivity regulate elastic recoil. This heterogeneity has also frustrated efforts to understand how single SF mechanics are related to the network properties in which they reside, even though this interconnectedness is broadly understood to play essential roles in cellular structure and motility.

Results

Single-cell ECM micropatterning represents a valuable tool for accomplishing this goal. The ability of this technology to arbitrarily standardize cell geometry has dramatically improved the field's understanding of how cell shape controls traction force, cytoskeletal architecture, proliferation/apoptosis, and stem cell fate (8, 19, 20). Micropatterning has also been used to prescribe the geometry of peripheral SFs (21–23). We reasoned that we could productively exploit micropatterning approaches to control cell and SF geometry in combination with SLA and thereby gain new insights into SF mechanics. We were first interested in

Significance

Actomyosin stress fiber (SF) networks transmit tension to the microenvironment, which contributes to cell shape and tissue assembly. However, virtually nothing is known about how SF geometry and network structure control the ability of an SF to generate tension. We normalized cell shape and SF length with micropatterning and used laser ablation to probe the viscoelastic properties of the resulting standardized SFs. We find that the retraction dynamics of a cut SF are strongly regulated by SF length, and this relationship may be amplified or offset by the orientation of the attached SFs in single cells as well as in a monolayer. Thus, SF force generation is controlled both locally via adhesive geometry and globally via connections to the actin network.

Author contributions: E.K., C.A.B., U.S.S., and S.K. designed research; E.K. and C.A.B. performed research; E.K., C.A.B., and U.S.S. contributed new reagents/analytic tools; E.K., C.A.B., U.S.S., and S.K. analyzed data; and E.K., C.A.B., U.S.S., and S.K. wrote the paper.

The authors declare no conflict of interest.

This article is a PNAS Direct Submission.

[1]To whom correspondence should be addressed. Email: skumar@berkeley.edu.

This article contains supporting information online at www.pnas.org/lookup/suppl/doi:10.1073/pnas.1606649114/-/DCSupplemental.

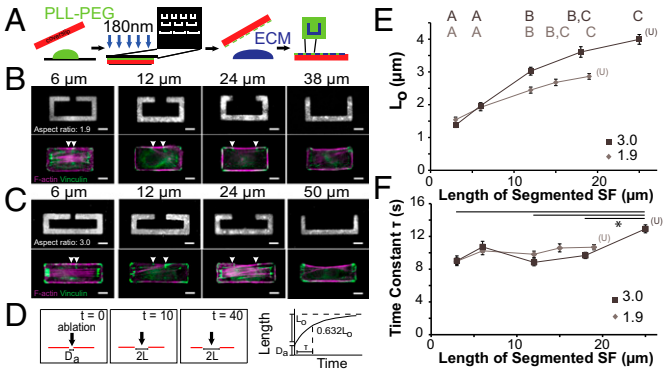

Fig. 1. Dissipation of elastic energy in severed SFs depends on fiber length. To elucidate SF mechanics and SF length relationships for fixed cell geometry, we created spacing patterns in which cells are cultured on patterns consisting of a rectangular frame that contains a variable-length gap. (*A*) Schematic of pattern fabrication. (*B*) (*Top*) FN distribution on patterns of aspect ratio 1.9 with gap lengths ranging from 6 to 38 μm. (*Bottom*) Distribution of F-actin (magenta) and vinculin (green) in U2OS cells seeded on the corresponding patterns. A length-defined SF is formed across the gap with focal adhesions formed at the ends. Gap ends depicted by white arrows. (*C*) (*Top*) FN stain on patterns of aspect ratio 3.0. (*Bottom*) F-actin and vinculin distributions. (*D*) SF retraction analysis. D_a, SF material destroyed by ablation; 2*L*, distance between fiber ends over time (*L* is the retraction distance of a severed SF fragment). Length *L* vs. time *t* is fit to the Kelvin–Voigt model to determine L_o, whose magnitude correlates with the SF's dissipated elastic energy, and τ, the viscoelastic time constant, which is the ratio of viscosity/elasticity. (*E*) Average L_o values for each pattern. A, B, and C statistical families show differences $P < 0.05$ determined using Dunn test for multiple comparisons of nonnormally distributed data. (*F*) Average τ values for each pattern. Statistical differences of $^*P < 0.05$ using Kruskal–Wallis followed by Dunn test ($N = 27$, 58, 89, 72, and 126 for each spacing of aspect ratio 1.9, and $n = 13$, 21, 38, 40, and 120 for each spacing of aspect ratio 3.0). Data points at 19 μm (aspect ratio 1.9) and 25 μm (aspect ratio 3.0) correspond to the U-shaped patterns (replotted from Fig. S1). Note that for the Kelvin–Voigt model, we measure the retraction of one end of the cut fiber, and as such, SF length is halved. (Scale bars, 10 μm.)

determining how SF length regulates viscoelastic retraction. To accomplish this, we designed three fibronectin (FN)-coated U-shaped patterns, i.e., patterns consisting of a rectangular frame of matrix with one long edge missing, of aspect ratios 1.5, 1.9, and 3.0 using a UV photopatterning strategy (Fig. 1*A* and Fig. 1 *B* and *C*, fourth column) (24). This strategy produced SFs of similar thickness with two terminal FAs and a length closely conforming to that of the pattern edge across all aspect ratios (Fig. S1 and Fig. 1 *B* and *C*, fourth column). We then applied SLA on SFs along the FN-free edge and observed their retraction kinetics. As in our previous studies, we fit each retraction curve to a Kelvin–Voigt viscoelastic cable model described by a time constant (τ), which reflects the SF's effective viscosity/elasticity ratio, and a plateau retraction distance (L_o), which correlates to the elastic energy dissipated by half of the severed SF (3, 17, 18) (Fig. 1*D*) (see *SI Text* and Fig. S2 for model choice). The retraction kinetics of these SFs exhibited a clear length dependence, with both L_o and τ ($P < 0.01$, Dunn test for nonparametric multiple comparison) increasing with length (Fig. S1). On the contrary, SFs produced on FN-filled rectangular patterns showed no statistical variation in dissipated elastic energy (L_o) or τ with SF length (Fig. S3) due to the presence of vinculin-positive FAs along the SF length, which pin the SF and prevent it from freely retracting (14). Thus, dissipated SF elastic energy and viscoelastic properties depend strongly on adhesive spacing, with longer SFs storing more elastic energy. These results validate indirect predictions from earlier micropattern-based studies on the elastic nature of SFs (21–23).

Earlier studies have shown that when area is conserved, cellular prestress increases with aspect ratio, raising concerns that these differences could contribute to the observed length dependence (19, 25). However, when we measured whole-cell RMS traction and strain energy on the varying aspect ratio U-shaped patterns, we did not observe differences (Fig. S4) (26). Nevertheless, to directly probe for SF mechanics rather than whole-cell prestress, we designed patterns in which the two parallel arms of the U are symmetrically but incompletely connected with matrix (spacing patterns), leaving a gap of defined length (6, 12, 24, and 30 μm for aspect ratio 1.9 and 6, 12, 24, and 36 μm for aspect ratio 3.0). Cells formed single SFs across the gap, with FAs present at the edge of each SF (Fig. 1 *B* and *C*). Dissipated elastic energy released by an SF (corresponding to L_o) did indeed scale with length, whereas τ remained relatively constant (Fig. 1 *E* and *F*). The length sensitivity of L_o decreased with increased SF length, which may be due to subtle differences in matrix geometry, SF connectivity, or prestress across these patterns. Additionally, at higher SF lengths, we observed differences in the elastic energy dissipated by SFs of equal length within cells of different aspect ratios (Fig. S5 for primary data).

As noted earlier, a key motivation for using single-cell micropatterning was to standardize SF geometry and facilitate the development of relationships between SF length and viscoelasticity. Despite this effort, we still observed experimental

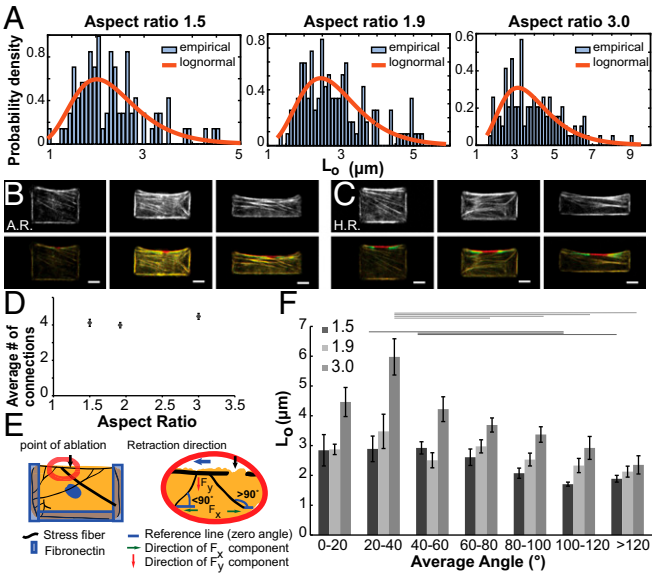

Fig. 2. Analysis of L_o distributions of U-shaped patterns reveals that elastic energy dissipation is heterogeneous and depends on network connectivity. (*A*) Probability density histograms of L_o on each U-shaped pattern fit to a lognormal distribution. (*B*) (*Top*) Preablation F-actin distribution (RFP-LifeAct) of average retracting (A.R.) cells whose L_o values fall under the peak. (*Bottom*) Overlay of F-actin distribution before (red) and after (green) ablation. (*C*) (*Top*) Preablation F-actin distribution of highly retracting (H.R.) cells whose L_o values fall under the tail of the fit. (*Bottom*) Overlay of actin network before (red) and after (green) ablation. (*D*) Dependence of number of connecting fibers to length-defined SF does not reveal statistical differences ($N = 66$, 94, and 103 for each aspect ratio, ANOVA followed by Tukey). Error bars represent SEM. (*E*) Schematic depicting angles with which the connecting fibers intersect the severed length-defined fiber. If the angle is between 0° and 90°, its cosine is positive and corresponds to an *x* component of the force (F_x) (green arrow) parallel to the direction of retraction (blue arrow). If the angle is between 90° and 180°, its cosine is negative resulting in an F_x that is antiparallel to the direction of retraction. Each cell is assigned an average angle value. (*F*) Correlation between observed L_o and average angle for a given cell. Bars are mean ± SEM, and lines portray statistical differences determined using ANOVA followed by Tukey ($P < 0.05$). (Scale bars, 10 μm.)

variation in SF retraction. Identifying remaining sources of heterogeneity could potentially yield valuable and unappreciated regulatory principles underlying SF mechanics. Indeed, when we examined our retraction distributions more closely, we noted that the L_o values were highly skewed on U-shaped patterns of all aspect ratios (Fig. 2*A*). The distributions closely follow lognormal distributions, with most cells falling under the peak and some cells falling under the long, right-sided tail of the fit (Fig. 2*A* and Table S1). The appearance of a lognormal distribution suggests that SF mechanical properties depend on their growth history. When we more closely inspected preablation and postablation RFP-LifeAct images for cells found under the peak (average retracting) and under the long tail (highly retracting) (Fig. 2 *B* and *C* and Fig. S6), we noted broad, cell-to-cell structural heterogeneities in the SF networks surrounding the target fiber. This in turn led us to hypothesize that variations in network structure might contribute to heterogeneities in SF viscoelasticity. We counted the number of SF connections to the length-defined SF (SF formed across the pattern gap) and found no statistical difference in the number of connections as a function of aspect ratio (Fig. 2*D*). We then asked whether the orientation of these connected SFs varies across cells. We hypothesized that connecting SFs apply a force on the length-defined SF whose *y* component (F_y; red arrow) is always downward and whose *x* component (F_x; green arrow) depends on the intersecting angle and location relative to the ablation site (Fig. 2*E*). Differences in angular distributions can presumably determine whether these connections and their corresponding forces are enhancing or impeding retraction. We calculated the average angle distribution per cell and binned the L_o values based on the average angle measurements (see Fig. S7 for examples of angle analysis). We first observed that for average angles >90°, L_o values are smaller compared with angles <90°, possibly due to the presence of an F_x value that is in the opposite direction of retraction (Fig. 2*F*). As the average angle distribution increases from 0° to 90°, we observed an increase in L_o that peaks around 20°– 40°. The presence of a peak suggests that retraction kinetics are affected by both the F_x and F_y imposed by connecting SFs. The angle of the connecting SF therefore contributes to dissipated elastic energy (L_o).

To experimentally test a causal role for SF connectivity in driving retraction, we performed gain- and loss-of-function studies with the myosin activator Rho-associated kinase (ROCK), which has been shown to govern SF assembly and contractility within the cellular interior, including the connecting SFs seen here. By contrast, peripherally located SFs such as the ones severed in our experiments are primarily regulated by myosin light chain kinase and are thus expected to be minimally perturbed by ROCK manipulation (17, 18). To suppress ROCK activity and dissipate central connections, we treated cells with 5 μM Y-27632. To enhance ROCK activity and strengthen connections, we stably overexpressed a constitutively active mutant of ROCK that is induced by doxycycline (CA-ROCK) (27) (Fig. S8). Immunostaining of FAs and SFs confirmed the increase of FA size in the presence of CA-ROCK and reduction in SF and FA formation in the presence of Y-27632 (Fig. 3*A*). In the absence of doxycyline, CA-ROCK cells have similar FAs to naive cells. Doxycycline addition induced the assembly of numerous SFs connected to the length-defined SF, whereas Y-27632–treated cells exhibited fewer connections (Fig. 3 *B* and *C*). The average number of connections per cell increased with CA-ROCK expression compared with naive and Y-27632–treated cells (Fig. 3*D*). To understand how these manipulations might influence the total F_y and F_x, we quantified the cell-to-cell distribution of the sums of the sines ($\sum \sin\alpha$ for F_y) and cosines ($\sum \cos\alpha$ for F_x) of the angles of intersection as defined earlier. Compared with naive cells, Y-27632 treatment shifted the $\sum \sin\alpha$ distribution to smaller values for all aspect ratios, whereas CA-ROCK expression shifted the distribution to larger values (Fig. 3*E*; $^*P < 0.05$ and $^{**}P < 0.001$). Similarly, Y-27632 treatment produced shifts to slightly more negative values for $\sum \cos\alpha$, and CA-ROCK overexpression led to more positive values (Fig. 3*F*; $^*P < 0.05$ and $^{**}P < 0.001$). When we performed SLA, we found that Y-27632 treatment reduced elastic energy dissipation (L_o) for all aspect ratios (relative to naive) and muted pattern to pattern differences. Conversely, CA-ROCK overexpression increased dissipated elastic energy compared with naive ($P < 0.05$ for 1.9 and 3) and enhanced pattern-to-pattern differences (Fig. 3*G*). With no doxycycline, CA-ROCK cells exhibited similar L_o values to naive U2OS RFP-LifeAct (Fig. S8). In parallel experiments, we found that wholesale inhibition of NMMII with blebbistatin reduced retraction distance while also producing an inward deflection of the length-defined SF (Fig. S9). This finding, together with our previous results, is consistent with our hypothesis that

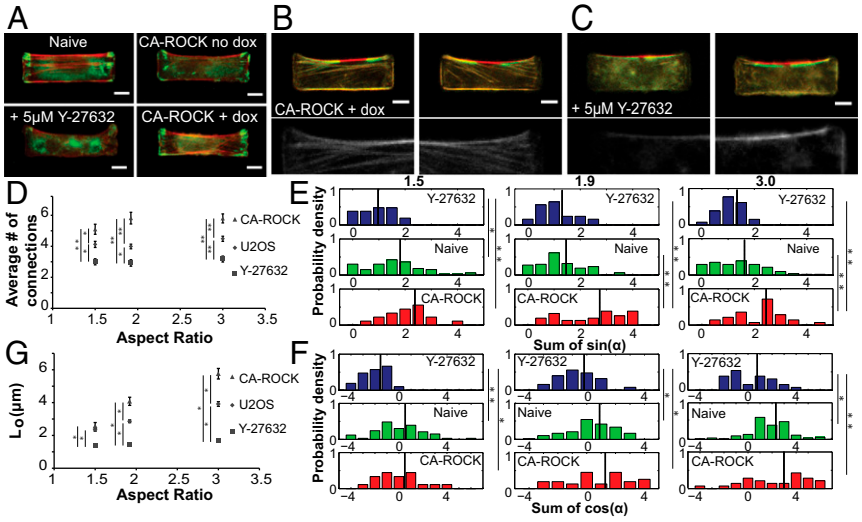

Fig. 3. Network control of SF retraction is regulated by Rho-associated kinase-mediated assembly of connecting fibers. (*A*) Vinculin (green) and SF (red) distributions in naive U2OS, U2OS pSLIK CA ROCK ± doxycycline, and Y-27632–treated U2OS cells (U-shaped patterns, aspect ratio 3.0). (*B* and *C*) Effect of CA ROCK and Y-27632 on SF architecture. (*Top*) SF distributions before (red) and after (green) ablation. (*Bottom*) High-magnification images of connecting fibers to length-defined SF. (*D*) Quantification of the average number of connecting fibers per cell (*N* for Y-27632 = 21, 27, and 28, and *N* for induced CA-ROCK = 20, 33, and 30 for each aspect ratio). Data points represent mean ± SEM. Statistical comparisons performed using ANOVA followed by Tukey ($^*P < 0.05$, $^{**}P < 0.001$). Data points for U2OS are transposed from Fig. 2*D*. (*E* and *F*) Histograms of $\sum \sin\alpha$ and $\sum \cos\alpha$ values per cell obtained for Y-27632, naive, and induced CA-ROCK cells per aspect ratio. Black lines depict the mean value. Statistical comparisons of cosine and sine distributions within same aspect ratio were performed using ANOVA followed by Tukey ($^*P < 0.05$, $^{**}P < 0.001$). (*G*) L_o for cells treated with Y-27632 (rectangles), induced CA-ROCK (triangles), and naive (diamonds) on each aspect ratio. *N* for Y-27632 = 21, 26, and 45, and *N* for induced CA-ROCK = 18, 33, and 30 for each aspect ratio. Data points for U2OS are transposed from Fig. S1. Data points are mean ± SEM. Statistical differences calculated using Dunn test for multiple comparison of nonnormal data ($^*P < 0.01$). (Scale bars, 10 μm.)

the viscoelastic properties of an SF are governed both by its own axial geometry and that of the network to which it connects.

To investigate causal relationships between network architecture and SF mechanics more precisely, we developed a simple mechanical model of networked elastic cables subjected to external force (Fig. 4*A*) (28, 29). Shapes and forces of peripheral SFs in the absence of connecting SFs have been previously described with the tension-elasticity model (TEM) (21). Peripheral SFs show a circularly invaginated shape due to the force balance of an elastic line tension λ and a homogenous surface tension σ (Fig. S10). We extended this model by including internal SFs that connect to the peripheral one and exert a force F_o at a prescribed angle α (*SI Text*). To simplify the model, we first considered a symmetric cell with one connecting SF at each side. Numerical solution of the system produces a distribution of F_{center} values with a peak at $\alpha \sim 70°$, reminiscent of our experimental observations. We explored the sensitivity of this solution to model parameters by varying the geometry of the system (connection point as determined by $l_{1,o}$), the active force (F_o), and the fiber stiffness EA (Fig. 4*B*). If the angle α is close to 0° or 180°, moving the connection points closer to the center (large $l_{1,o}$) does not affect the force calculated. For intermediate values of α, however, the force increases with increased $l_{1,o}$ (Fig. 4*B*, *Top*). In contrast, varying the active force F_o changes both the basal and maximal force values (Fig. 4*B*, *Middle*). Changing the SF stiffness leaves the force levels unchanged for both large and small α (Fig. 4*B*, *Bottom*). Based on this simple symmetric model, we conclude that the magnitude of F_o is not the sole determinant for predicting the dissipated elastic energy of a length-defined SF. Instead, the force F_o has both an x component in the direction of retraction and a y component in the normal direction that pulls on the severed SF. This pull distends the retracting SF, introducing an additional elastic component that further enhances retraction. Without this y component force and the additional spring, SFs would retract maximally at $\alpha = 0$, a prediction not consistent with our experimental observations. The presence of this elastic force is further confirmed by our experimental observation that the length-defined SF moves outward following SLA of the internal connecting fibers showing that connecting fibers contribute through prestress (Fig. S11).

To further understand how connecting fibers contribute to local retraction within a single SF, we photobleached fiduciary markers in a single SF, photoablated the SF, and followed the retraction of each intermarker segment. When an SF fragment was highly connected at acute angles, SF segments within that fragment retracted more than those in the nonconnected SF fragment (Fig. S12 *A* and *C*). However, when an SF fragment was connected at large angles (>90°), SF segments underwent smaller retraction than the nonconnected SF fragment (Fig. S12*B*). Based on our results and our simple active cable model, we conclude that differences in the location and angle of connecting fibers can explain cell to cell heterogeneities in the elastic energy dissipated by SFs after SLA.

The symmetry inherent in our model (Fig. 4*A*) represents a major simplification of cellular SF networks. To test whether this reasoning could be extended to more complex experimentally observed SF distributions, we manually traced the location and angle of connecting SFs in a population of cells and generated a triangular mesh network that embeds the SFs as marked edges (Fig. 4 *C*–*E*). For illustration, we calculated the equilibrium force distribution for the length-defined SF using active force F_o= 5 nN and EA = 500 nN. Although a connecting SF adds only 5 nN of active force, the total force in the length-defined SF is as high as 25 nN at the center where SLA occurs and exhibits a heterogeneous energy distribution depending on the connecting SFs (Fig. 4*E*). To find optimal parameters for both active force and stiffness, we carried out active cable network simulations based on two data sets ($n = 8$ and $n = 5$ cells cultured on U-shaped patterns with aspect ratios of 1.9 and 3.0, respectively). Within each data set, we used the same parameters for all cells. Thus, the differences in the predicted forces between cells on the same pattern arise solely from the geometry of the internal SF distribution. To convert forces retrieved from the model to retraction distances L_f using a simple spring model ($k = 3$ nN/μm), we adjusted F_o and EA for all cells in the data set to achieve optimal agreement with experiments. We found that connecting SF geometries are sufficient to explain the differences in retraction within each data set (Fig. 4*F*), although not with the same parameters for both aspect ratios. In contrast, we observed that SFs are both stiffer ($EA_{r\,=\,1.9} = 40$ nN compared with $EA_{r\,=\,3.0} = 80$ nN) and more contractile ($F_{o\,r\,=\,1.9} = 4$ nN and $F_{o\,r\,=\,3.0} = 7$ nN) at aspect ratio 3.0. Thus, a simple model that considers SF networks as a series of connected elastic cables enables us to dissect differences in the mechanical properties of SFs and accurately predict the retracted distance of a peripheral SF based only on its connections to other SFs.

To test whether the concepts developed with patterned single cells can also be extended to multicellular structures in which SF networks may be physically integrated across several cells, we performed SLA on cells grown in a monolayer (Fig. 5 *A* and *B*). Quantification of retraction kinetics showed that the relationship between SF length and retraction distance observed in patterned single cells (Fig. 1*E*) holds true in a monolayer setting: increasing SF

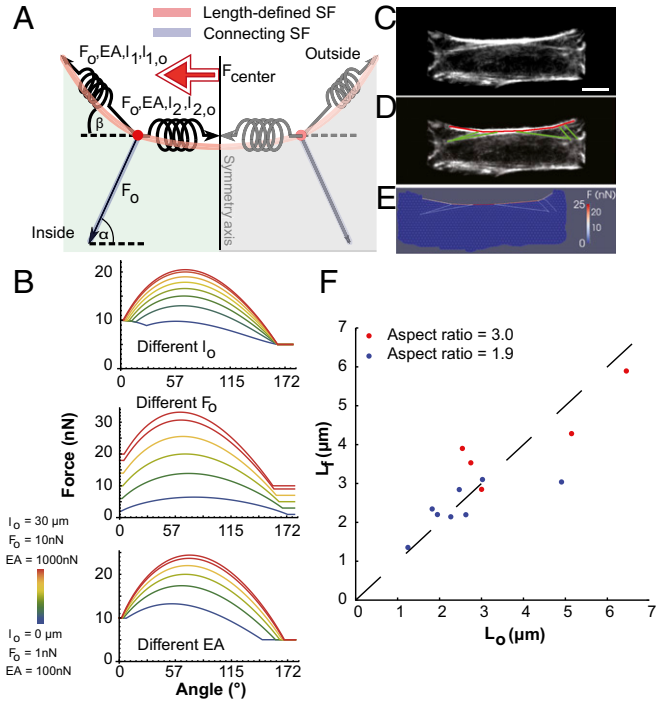

Fig. 4. An active cable network (ACN) model recapitulates key experimental results. (*A*) Symmetric model in which connecting SFs are modeled as exerting an active force F_o and defined-length SFs are modeled as active elastic cables. (*B*) Parametric studies relating the magnitude of F_{center} to changes in geometry ($l_{1,o}$), SF active tension (F_o), and SF stiffness (EA). All curves exhibit the same shape and show that intermediate angles (60°–100°) support the greatest force, which is due to the additional elastic component of the length-defined SF from the pull of the internal F_o that stretches the spring of the length-defined SF. (*C*–*E*) Segmentation process of the ACN model. U2OS RFP-LifeAct images obtained before SLA were manually segmented and SF network simulations are created as discussed in *SI Text*. (*F*) Plot of simulated retraction lengths L_f (y axis) against experimentally derived retraction lengths L_o (x axis) ($n = 8$ and 5 for aspect ratios 1.9 and 3.0, respectively). Parameters used for ACN are as follows: $F_o = 4$ nN, EA = 40 nN at aspect ratio 1.9 and $F_o = 7$ nN, and EA = 80 nN at aspect ratio 3.0.

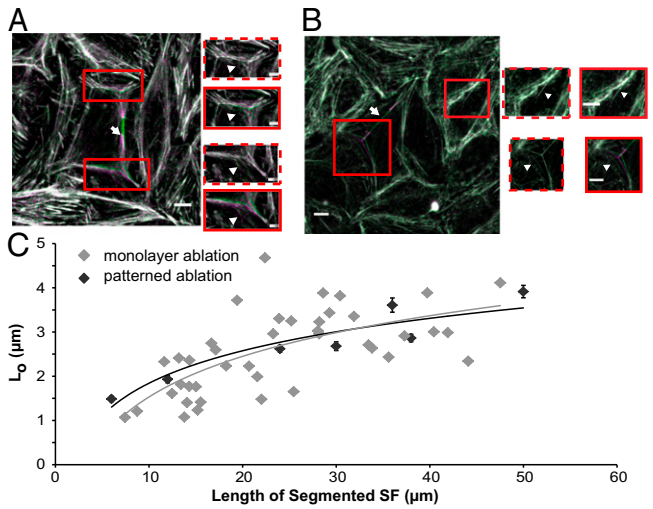

Fig. 5. Dissipation of elastic energy in a monolayer setting is related to SF length and connectivity. To elucidate whether the relationships uncovered using patterned single cells hold true in nonpatterned cells, we performed SLA of SFs in cells grown as a monolayer. (*A* and *B*) Examples of an ablated SF within cells that are growing in a monolayer. Overlay of cells before (green) and after ablation (magenta). Solid red boxes show overlay of images before (green) and after (magenta) ablation. Dashed red boxes show overlay of images taken at different times with no ablation to control for any SF movement during imaging. Arrowheads within solid red boxes point to regions of increased SF network rearrangement. In *B*, the ablated SF is highly connected and therefore undergoes large retraction, which leads to SF network rearrangements within cells farther away from the site of ablation (arrowheads within solid red boxes). (*C*) Overlay of patterned single-cell retraction kinetics (data transposed from Fig. 1*E*) and monolayer ablation retraction kinetics (gray diamonds). Both single-cell and monolayer ablation results exhibit similar relationships between SF length and dissipated elastic energy after SLA. (Scale bars are 10 μm for all images except zoomed-in images in *A*, where scale bars are 5 μm.)

length leads to increased L_o, reaching an eventual plateau (Fig. 5*C*). Remarkably, the effect of connectivity is amplified in the presence of cell–cell adhesions, as evidenced by the transmission of tension release from the targeted cell to its nearest neighbors. In some instances, this tension release is felt within distant cells tens of micrometers away (Fig. 5*B* and Movies S1 and S2).

Finally, we wondered whether changes in SF connectivity might contribute to broader cell-scale functions such as directional motility. To study the effect of connectivity on migration, we stimulated patterned cells using epidermal growth factor (EGF) to initiate the formation of migratory processes (20). When cells grown on the spacing patterns of aspect ratio 1.9 were EGF-stimulated, migratory processes were formed in ways that depended on the gap length (Fig. S13): for small gaps, migratory processes were formed at either the spacing side or the FN side, whereas for larger gaps, migratory processes only formed at the FN side, leading to a polarized cell with a rear SF. Moreover, the rear SFs of EGF-stimulated cells on U-shaped patterns (aspect ratio 1.5 and 1.9) exhibited increased connectivity with more internal SFs connecting to them (Fig. 6 *A* and *B*). When comparing the average angle distribution of naive versus EGF-treated cells, we observed a decrease in the average angle, which suggests that under EGF treatment, cells rearrange their SF networks to both increase the number of connections and align these connecting SFs at more acute angles (Fig. S14). Connectivity analysis revealed increases in both $\sum\cos\alpha$ and $\sum\sin\alpha$ distributions for both aspect ratios (Fig. 6*C*; $^{**}P < 0.001$) due to both the change in the angle of connecting fibers and the increase in the number of connections. Based on the broader force distributions, we hypothesized and observed that the rear SFs of EGF-treated cells dissipate increased elastic energy after ablation (Fig. 6*D*; $^{**}P < 0.001$). Our results suggest that as the cell is induced to migrate, SF connectivity evolves to suit the tensile/contractile needs of the rear SF, resulting in changes in SF mechanical properties as measured by SLA.

Discussion

In this study, we have combined single-cell micropatterning and SLA to elucidate how SF geometry and connections within a complex network alter the elastic energy dissipated by an SF. Previous studies have produced several models that suggest that retraction length scales with SF length but make no predictions on how SF contractility and stiffness vary with SF length (14–16). Our results show that the relationship between SF length and dissipated elastic energy after SLA is more complex than previously appreciated and offers insights into this intricate relationship.

First, simulations demonstrate that longer SFs are stiffer and more contractile, a result that would not be predicted by existing SF models. Second, we do not find a simple linear increase, as suggested by simple mathematical models for SF retraction (*SI Text*), but a decrease in slope with increasing SF length. This is an insight that could be due to the interconnectedness of the actin SF network. Our study shows that the presence of internal connections leads to inhomogeneous retraction within the same SF as well as heterogeneities across standardized cells. In addition to producing prestress on the length-defined SF, differences in connectivity may also affect τ due to differences in drag force, in that a highly connected SF pulls a greater subset of the actin cytoskeleton as it retracts, effectively increasing viscous drag (Fig. S15). Our results directly show that connecting fibers, rather than the viscosity of the cytosol, dominate the viscous component of the retraction, thereby resolving an important open-ended question in the field of SF mechanics (15).

Furthermore, when we cut single SFs in a monolayer setting, we observed tension release and SF rearrangement in distant cells. Recent work has suggested that transmission of contractile

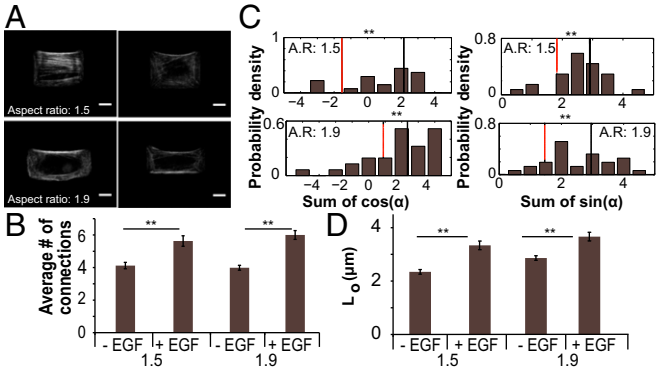

Fig. 6. U2OS RFP-LifeAct cells treated with EGF acquire a motile phenotype where the rear SF exhibits increased connectivity and increased elastic energy. (*A*) U2OS RFP-LifeAct cells seeded on U patterns treated with EGF. (*B*) Quantification of the average number of connecting fibers per cell (*N* for EGF treatment = 27 and 31 for each aspect ratio). Data points represent mean ± SEM. Data for non-EGF–treated cells are transposed from Fig. 3*D*. Statistical comparisons performed using two-way Student *t* test ($^{**}P < 0.001$). (*C*) Histograms of (*Left*) $\sum\cos\alpha$ and (*Right*) $\sum\sin\alpha$ values per cell obtained for EGF-treated cells grown on U patterns of aspect ratio 1.5 (*Top*) and aspect ratio 1.9 (*Bottom*). Black lines depict the mean value of EGF-treated cells, and red lines depict the mean value of non-EGF–treated cells (averages transposed from Fig. 3 *E* and *F*). Statistical comparisons of cosine and sine distributions within same aspect ratio were performed using two-way Student *t* test ($^{**}P < 0.001$). (*D*) L_o for cells treated with EGF on each aspect ratio. $n = 44$ and 48 for EGF-treated cells for each aspect ratio. Data points are mean ± SEM. Statistical differences calculated using two-way Student *t* test ($^{**}P < 0.001$). Data for non-EGF–treated cells are transposed from Fig. S1. (Scale bars, 10 μm.)

forces between cells critically regulates collective migration and durotaxis. Much of the evidence for this concept has been indirectly inferred from whole-cell traction force and genetic and pharmacological manipulations of cadherins and myosin (30–33). Our findings now provide direct evidence that single cytoskeletal structures in cells mediate tensile forces over long distances across a monolayer. Our results also provide mechanistic insight into how aggregates of cells can cooperatively generate outsize traction forces, which is important in collective cell migration and matrix remodeling (30).

Although our cable network model was quite minimalistic and only incorporated a small portion of the cytoskeletal network, it successfully predicted key experimental results and achieved remarkable quantitative agreement with the experimental results for specific cells. This suggests that cellular geometry and SF network properties are the primary drivers of SF viscolelastic retraction, whatever other cell-to-cell variations in structure or mechanics may exist. Precisely how SF network heterogeneities arise and evolve represents an important open question, and it is possible that this may be a function of the cell's adhesive and spreading history. Indeed, our findings complement the recent, elegant demonstration that patterning reconstituted actomyosin network architecture can modulate contractility (34). Development of analogous micropatterning strategies for living cells may make it possible to test the hypotheses raised in our study by engineering the details of the internal SF network through strategic placement of adhesions.

Materials and Methods

Cell Lines and Reagents. Viral particles of the pFUG-RFP-LifeAct vector were packaged in 293T cells and used to infect U2OS cells (ATCC HBT-96) (35). Cells were cultured in DMEM with 10% (vol/vol) FBS (JR Scientific), 1% penicillin/strep (Thermo Fisher Scientific), and 1% nonessential amino acids (Life Technologies).

Confocal Imaging of Immunofluorescence and SF Photodisruption. Immunostaining imaging and SF SLA experiments were performed on a Zeis LSM 510 Meta Confocal microscope equipped with a MaiTai Ti:sapphire femtosecond laser (Spectra Physics) (9, 17, 18).

Deep UV-Based Pattern Fabrication. Patterns were made as described elsewhere (24) and as shown in Fig. 1*A*.

See *SI Materials and Methods* for details on all methods and data analysis.

ACKNOWLEDGMENTS. The authors acknowledge Prof. Manuel Thery and Dr. Timothée Vignaud for valuable technical guidance on patterning methods. This work was performed in part at the Cancer Research Laboratory Molecular Imaging Center supported by National Institutes of Health (NIH) Grant 3R01EY015514-01S1. E.K. and C.A.B. gratefully acknowledge the support of the Howard Hughes Medical Institute International Student and Siebel Scholar fellowships and Konrad Adenauer Foundation fellowship, respectively. This work was supported by the NIH (1R21EB016359), the National Science Foundation (CAREER Award CMMI-1055965), and the France–Berkeley Fund. C.A.B. and U.S.S. acknowledge support by the Heidelberg Karlsruhe Research Partnership. U.S.S. is a member of the cluster of excellence CellNetworks and the Interdisciplinary Center for Scientific Computing.

1. Burnette DT, et al. (2014) A contractile and counterbalancing adhesion system controls the 3D shape of crawling cells. *J Cell Biol* 205(1):83–96.
2. Kassianidou E, Kumar S (2015) A biomechanical perspective on stress fiber structure and function. *Biochim Biophys Acta* 1853(11, Part B):3065–3074.
3. Kumar S, et al. (2006) Viscoelastic retraction of single living stress fibers and its impact on cell shape, cytoskeletal organization, and extracellular matrix mechanics. *Biophys J* 90(10):3762–3773.
4. Zemel A, Rehfeldt F, Brown AEX, Discher DE, Safran SA (2010) Cell shape, spreading symmetry and the polarization of stress-fibers in cells. *J Phys Condens Matter* 22(19): 194110.
5. Zeng Y, et al. (2015) Formin-like2 regulates Rho/ROCK pathway to promote actin assembly and cell invasion of colorectal cancer. *Cancer Sci* 106(10):1385–1393.
6. Darby IA, Laverdet B, Bonté F, Desmoulière A (2014) Fibroblasts and myofibroblasts in wound healing. *Clin Cosmet Investig Dermatol* 7:301–311.
7. Blanchoin L, Boujemaa-Paterski R, Sykes C, Plastino J (2014) Actin dynamics, architecture, and mechanics in cell motility. *Physiol Rev* 94(1):235–263.
8. Makhija E, Jokhun DS, Shivashankar GV (2016) Nuclear deformability and telomere dynamics are regulated by cell geometric constraints. *Proc Natl Acad Sci USA* 113(1): E32–E40.
9. Chang C-W, Kumar S (2013) Vinculin tension distributions of individual stress fibers within cell-matrix adhesions. *J Cell Sci* 126(Pt 14):3021–3030.
10. Kovac B, Teo JL, Mäkelä TP, Vallenius T (2013) Assembly of non-contractile dorsal stress fibers requires α-actinin-1 and Rac1 in migrating and spreading cells. *J Cell Sci* 126(Pt 1):263–273.
11. Tojkander S, Gateva G, Husain A, Krishnan R, Lappalainen P (2015) Generation of contractile actomyosin bundles depends on mechanosensitive actin filament assembly and disassembly. *eLife* 4:e06126.
12. Katoh K, Kano Y, Masuda M, Onishi H, Fujiwara K (1998) Isolation and contraction of the stress fiber. *Mol Biol Cell* 9(7):1919–1938.
13. Thoresen T, Lenz M, Gardel ML (2013) Thick filament length and isoform composition determine self-organized contractile units in actomyosin bundles. *Biophys J* 104(3): 655–665.
14. Colombelli J, et al. (2009) Mechanosensing in actin stress fibers revealed by a close correlation between force and protein localization. *J Cell Sci* 122(Pt 10):1665–1679.
15. Stachowiak MR, O'Shaughnessy B (2009) Recoil after severing reveals stress fiber contraction mechanisms. *Biophys J* 97(2):462–471.
16. Russell RJ, Xia S-L, Dickinson RB, Lele TP (2009) Sarcomere mechanics in capillary endothelial cells. *Biophys J* 97(6):1578–1585.
17. Chang C-W, Kumar S (2015) Differential contributions of nonmuscle myosin II isoforms and functional domains to stress fiber mechanics. *Sci Rep* 5:13736.
18. Tanner K, Boudreau A, Bissell MJ, Kumar S (2010) Dissecting regional variations in stress fiber mechanics in living cells with laser nanosurgery. *Biophys J* 99(9): 2775–2783.
19. Rape AD, Guo WH, Wang YL (2011) The regulation of traction force in relation to cell shape and focal adhesions. *Biomaterials* 32(8):2043–2051.
20. Parker KK, et al. (2002) Directional control of lamellipodia extension by constraining cell shape and orienting cell tractional forces. *FASEB J* 16(10):1195–1204.
21. Bischofs IB, Klein F, Lehnert D, Bastmeyer M, Schwarz US (2008) Filamentous network mechanics and active contractility determine cell and tissue shape. *Biophys J* 95(7): 3488–3496.
22. Labouesse C, Verkhovsky AB, Meister J-J, Gabella C, Vianay B (2015) Cell shape dynamics reveal balance of elasticity and contractility in peripheral arcs. *Biophys J* 108(10):2437–2447.
23. Labouesse C, Gabella C, Meister J-J, Vianay B, Verkhovsky AB (2016) Microsurgery-aided in-situ force probing reveals extensibility and viscoelastic properties of individual stress fibers. *Sci Rep* 6:23722.
24. Azioune A, Carpi N, Tseng Q, Théry M, Piel M (2010) Protein micropatterns: A direct printing protocol using deep UVs. *Methods Cell Biol* 97(10):133–146.
25. Oakes PW, Banerjee S, Marchetti MC, Gardel ML (2014) Geometry regulates traction stresses in adherent cells. *Biophys J* 107(4):825–833.
26. Mertz AF, et al. (2012) Scaling of traction forces with the size of cohesive cell colonies. *Phys Rev Lett* 108(19):198101.
27. Wong SY, et al. (2015) Constitutive activation of myosin-dependent contractility sensitizes glioma tumor-initiating cells to mechanical inputs and reduces tissue invasion. *Cancer Res* 75(6):1113–1122.
28. Guthardt Torres P, Bischofs IB, Schwarz US (2012) Contractile network models for adherent cells. *Phys Rev E Stat Nonlin Soft Matter Phys* 85(1 Pt 1):011913.
29. Soiné JRD, et al. (2015) Model-based traction force microscopy reveals differential tension in cellular actin bundles. *PLoS Comput Biol* 11(3):e1004076.
30. Sunyer R, et al. (2016) Collective cell durotaxis emerges from long-range intercellular force transmission. *Science* 353(6304):1157–1161.
31. Ng MR, Besser A, Danuser G, Brugge JS (2012) Substrate stiffness regulates cadherin-dependent collective migration through myosin-II contractility. *J Cell Biol* 199(3): 545–563.
32. Fernandez-Gonzalez R, Simoes S de M, Röper J-C, Eaton S, Zallen JA (2009) Myosin II dynamics are regulated by tension in intercalating cells. *Dev Cell* 17(5):736–743.
33. Ng MR, Besser A, Brugge JS, Danuser G (2014) Mapping the dynamics of force transduction at cell-cell junctions of epithelial clusters. *eLife* 3:e03282.
34. Ennomani H, et al. (2016) Architecture and connectivity govern actin network contractility. *Curr Biol* 26(5):616–626.
35. Lee JP, Kassianidou E, MacDonald JI, Francis MB, Kumar S (2016) N-terminal specific conjugation of extracellular matrix proteins to 2-pyridinecarboxaldehyde functionalized polyacrylamide hydrogels. *Biomaterials* 102:268–276.
36. Murrell M, Oakes PW, Lenz M, Gardel ML (2015) Forcing cells into shape: The mechanics of actomyosin contractility. *Nat Rev Mol Cell Biol* 16(8):486–498.
37. Besser A, Schwarz US (2007) Coupling biochemistry and mechanics in cell adhesion: A model for inhomogeneous stress fiber contraction. *New J Phys* 9(11):425.
38. Stachowiak MR, O'Shaughnessy B (2008) Kinetics of stress fibers. *New J Phys* 10(2): 25002.
39. Besser A, Colombelli J, Stelzer EHK, Schwarz US (2011) Viscoelastic response of contractile filament bundles. *Phys Rev E Stat Nonlin Soft Matter Phys* 83(5 Pt 1):051902.
40. Mayer M, Depken M, Bois JS, Jülicher F, Grill SW (2010) Anisotropies in cortical tension reveal the physical basis of polarizing cortical flows. *Nature* 467(7315):617–621.
41. Bischofs IB, Schmidt SS, Schwarz US (2009) Effect of adhesion geometry and rigidity on cellular force distributions. *Phys Rev Lett* 103(4):048101.